

Atmospheric and oceanic responses to Super Typhoon Mangkhut in the South China Sea: a coupled CROCO-WRF simulation*

Mingyu LI¹, Yijun HE^{1, **}, Guoqiang LIU^{1, 2, 3, 4}

¹ School of Marine Sciences, Nanjing University of Information Science and Technology, Nanjing 210044, China

² Marine Science and Engineering Guangdong Laboratory, Zhuhai 519000, China

³ Department of Engineering Mathematics and Internetworking, Dalhousie University, Halifax B3H 4R2, Canada

⁴ Bedford Institute of Oceanography, Fisheries and Oceans Canada, Dartmouth B2Y 4A2, Canada

Received Oct. 10, 2021; accepted in principle Mar. 31, 2022; accepted for publication May 7, 2022

© Chinese Society for Oceanology and Limnology, Science Press and Springer-Verlag GmbH Germany, part of Springer Nature 2023

Abstract The South China Sea (SCS) is the largest marginal sea in the Northwest Pacific Ocean, and it encounters frequent typhoons. The atmosphere and ocean will create significant thermal and dynamic responses during the intense disturbance caused by typhoons. However, these responses have not been thoroughly investigated owing to the complicated marine environment. According to the satellite data, the SCS Basin was observed to have a strong sea surface temperature (SST) response to Typhoon Mangkhut, resulting in widespread SST cooling. A coupled model was used to investigate the atmospheric and oceanic responses to Typhoon Mangkhut. Best-track data, satellite SST, and ARGO measurements show that the coupled WRF-CROCO simulation displays better track, intensity, SST, temperature, and salinity profiles than those of the WRF-only simulation. Results show that the typhoon induced rightward intensifications in wind speed, ocean current, and SST. The following are some remarkable atmosphere and ocean responses: (1) the SST below the inner-core region is cooled by 1 °C, resulting in a 37%–44% decrease in wet enthalpy, and the central pressure is increased by ~9 hPa. Therefore, the changes in SST below the inner-core region of the SCS Basin have a significant impact on air-sea fluxes under high-wind conditions; (2) the ocean boundary layer analysis shows that near-inertial oscillations on the right side of the typhoon track and a strong inertial current up to ~2.28 m/s in the upper ocean were observed, which resonated with the local wind and flow field on the right side and induced strong SST cooling; (3) a decrease in SST decreased the moist static energy of the typhoon boundary layer, thereby weakening the typhoon's intensity. The difference in equivalent potential temperature and sea surface pressure have a good correlation, indicating that the influence of moist static energy on typhoon intensity cannot be overlooked.

Keyword: Super Typhoon Mangkhut; coupled ocean-atmosphere model; wet enthalpy; inertial current

1 INTRODUCTION

Typhoons are strong cyclonic vortexes with a warm-core structure, and they have a rapid and serious impact on the atmosphere and marine environment through the heat and momentum transfer at the air-sea interface. A typhoon is not only a wind disaster but also causes beach erosion and storm surge (forming a typhoon disaster chain that seriously affects marine operations) (Peduzzi et al., 2012; Ge et al., 2017).

The typhoon-ocean interaction is manifested in

the violent exchange of energy and mass between the ocean and the atmosphere. The responses of the ocean to the typhoon can be divided into two parts: thermodynamic and dynamic responses. The thermodynamic responses are the changes in ocean temperature, salinity, and ecological parameters caused by strong wind stress, heavy precipitation

* Supported by the National Natural Science Foundation of China (No. 41620104003) and the Postgraduate Research and Practice Innovation Program of Jiangsu Province (Nos. SJKY19_0951, KYCX21_0959)

** Corresponding author: yjhe@nuist.edu.cn

and heat flux, whereas the dynamic responses are the seawater flows caused by strong wind stress and sea surface pressure gradient. Sea surface temperature (SST) cooling is a prominent aspect of ocean thermal response. In the northern hemisphere, the SST cooling is usually stronger on the right side of the typhoon path, with a cooling range of 1–9 °C (Chiang, 2011; Ko et al., 2014). In the marginal sea areas, the SST cooling can even reach 11 °C, leading to the reversal of sensible and latent heat flux (Price, 1981; Price et al., 1983; Emanuel, 1999; Wu et al., 2018, 2020; Sian et al., 2020). The extent of SST cooling depends on the depth of the mixed layer (ML) of the ocean and the stratification capacity of the thermocline prior to the storm (Black and Dickey, 2008; Mei et al., 2015). A fast-moving typhoon is a strong disturbance of the atmosphere to the ocean, which produces violent dynamic responses. One prominent dynamic response is near-inertial oscillations (NIOS), which are characterized by oscillating horizontal near-inertial currents (NICs) (Price, 1983; Liu et al., 2011). The depth of an ML and thermocline are influenced by the NICs caused by wind forces. The shear and instability of the NICs are the main reasons for the enrolling of low-temperature seawater under the ML, surface cooling, and ML deepening (Hormann et al., 2014). In addition to the oceanic responses, the atmospheric response to the ocean is also dramatic, and the ocean has a considerable impact on the structure and heat flux of the typhoon. At the air-sea interface, a strong exchange of mass and energy is observed, especially the exchange of wet enthalpy (sensible heat + latent heat). The wet enthalpy transported from the ocean

to the atmosphere is an important energy source for typhoon maintenance and development. In addition to the wet enthalpy, one prominent thermal atmospheric response is the equivalent potential temperature (θ_e). Driven by the pressure, the air mass in the outer boundary layer of the typhoon moves to its inner-core region, and the energy obtained from the ocean is continuously conveyed to the center of the typhoon, causing the low altitude (θ_e) to rise continuously in the center of the typhoon. If $\frac{\partial \theta_e}{\partial z} < 0$, the gas layer would be convective and unstable. This “potential” unstable gas layer was uplifted and transformed into a real unstable gas layer because of a certain triggering mechanism. In the deep convective region, the water vapor with high temperature, humidity, and energy in the lower layer was quickly carried to the upper troposphere, which provided energy for the maintenance and development of the typhoon (Cione and Uhlhorn, 2003; Zhu and Zhang, 2006).

The South China Sea (SCS) is a semi-enclosed sea basin connected to the Northwest Pacific Ocean and the East China Sea (ECS) through the Luzon Strait and Taiwan Strait in the north. The SCS participated in the evolution of the Indonesian through-stream through the Karimata Strait and the Mindoro Strait in the south. The SCS has a broad continental shelf in the north and a central basin with a depth of >4 000 m (Fig.1a). On average, the SCS produces and encounters more than ten typhoons each year, causing landfalls over the mainland of China or the Indochina Peninsula. Improving the accuracy of typhoon forecasting, especially in the

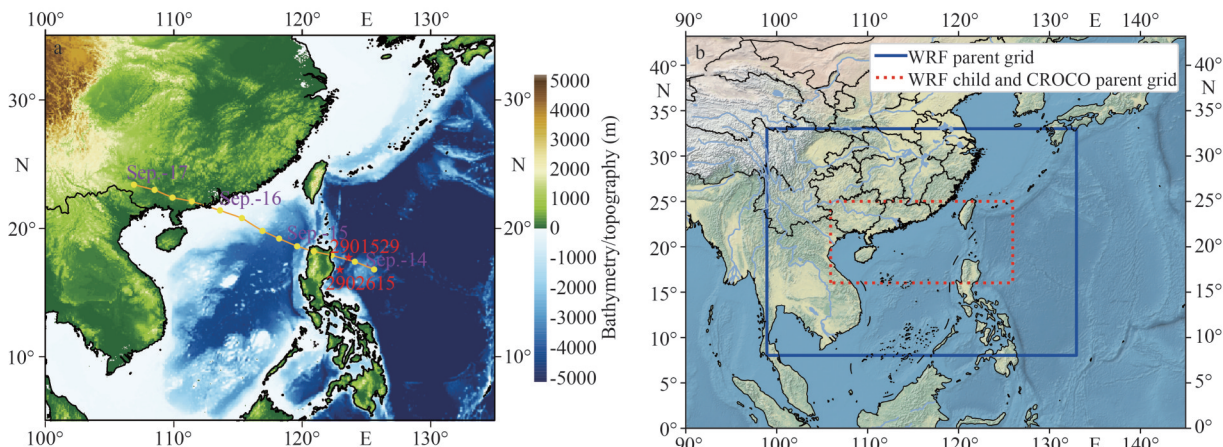


Fig.1 Topography (a) of the South China Sea (SCS) and simulated domains (b)

The background color represents the terrain elevation (m). The red five-pointed star shows the positions of Buoy 2902615 and 2901529. The orange line represents Super Typhoon Mangkhut's track between 09-14-2018 06:00:00 UTC and 09-17-2018 06:00:00 UTC with 6-h intervals derived from the JTWC data. Map review No. GS(2021)5444.

SCS, is critical for protecting maritime shipping and the safety of life and property of the coastal residents. The prediction of typhoons has improved over the past decades owing to the increased high-quality satellite data assimilation and the deepened understanding of typhoon structures and dynamic processes. However, the improvement in typhoon intensity prediction is not significant (Rogers et al., 2006; Bender et al., 2007; Demaria et al., 2014). The typhoon intensity prediction can be considerably limited by inaccurate initial fields, coarse numerical model resolution, an inaccurate descriptions of the dynamic process of the typhoon's inner core region, and especially a lack of understanding of the atmospheric and oceanic responses to typhoons.

Studies on the responses of the SCS to typhoons mainly focused on some prominent characteristics of dynamics or thermodynamics, such as using mooring acoustic Doppler current analyzer data to explore the NIOs (Chen et al., 2013; Yang and Hou, 2014). However, owing to the relative lack of ocean observation data, the numerical models provide another method for studying the atmospheric and oceanic responses. Chu et al. (2000) used the Princeton Ocean Model (POM) to simulate the response process of the upper ocean when Typhoon Ernie (1996) passed over the SCS and concluded that the responses of the offshore to the typhoon were similar to those of the open ocean, they adopted the empirical model wind field without considering the coupling effect of ocean and atmosphere. Xu et al. (2020) investigated the oceanic responses caused by Typhoon Rananim (2004) using the MIT General Circulation Model (MITgcm) driven by similar wind data. Owing to the low resolution of the reanalysis data used, the typhoon intensity may be considerably underestimated, making it difficult to obtain the properly resolved typhoon structure. Some studies (Chen et al., 2007; Gronholz et al., 2017) show that typhoon evolution is affected by many complex physical factors, and it is difficult to accurately simulate using a single ocean model, but the coupling of the atmosphere and the ocean is a pivotal approach to solve these problems. Bender and Ginis (2000) established a high-precision air sea coupled model based on the Geophysical Fluid Dynamics Laboratory (GFDL) three-layer moving nested hurricane model and POM ocean model to investigate the oceanic responses and argued that the SST feedback has a great impact on the hurricane intensity. However, their coupling model lacked some proper parameterizations or coarse resolutions

(Chen et al., 2013; Pianezze et al., 2018). Extensive studies are available on the responses of the SCS to typhoons, but the responses of the SCS Basin along the track are yet to be explored (Sun et al., 2012; Yang and Hou, 2014; Emanuel, 2017; Zheng et al., 2017). This can be attributed to the following factors. (1) The presence of complex spatial structure and evident seasonal variation with multiple mesoscale vortices in the circulation field owing to the influence of the SCS Basin monsoon and complex topography. (2) The inconsideration of oceanic and atmospheric dynamic processes and the use of coarse model resolution. (3) Data loss and inefficiency of infrared satellite SST retrieval because of the clouds above the SCS Basin.

Super Typhoon Mangkhut was the most influential and intense tropical cyclone (TC) in 2018 in the North Pacific and SCS Basin, and it had a long lifespan. The infrared (MODIS, GAC) and merged cloud-penetrating microwave data demonstrate the response of SST to Mangkhut in the SCS basin (Fig.2). Presently, most studies on the response of the SCS Basin to typhoons focus on the oceanic responses, especially the upper ocean whereas the analysis of the atmospheric responses is limited (Sun et al., 2012; Guan et al., 2014). To reveal the atmospheric and oceanic responses to Mangkhut more extensively, numerical simulations were conducted under dynamic oceanic and atmospheric conditions. This paper used a coupled ocean-atmosphere model (i.e., weather research and forecasting (WRF)-coastal and regional ocean community (CROCO)) to investigate the atmospheric and oceanic responses to Mangkhut.

The remainder of this paper is arranged as follows: Section 2 presents the evolution of Super Typhoon Mangkhut and satellite SST response to Mangkhut. Section 3 describes the datasets used in this study and the detailed description of the coupled model's configuration. Section 4 describes the simulation verification of the model. Section 5 provides results and discussion of the atmospheric and oceanic responses to Super Typhoon Mangkhut. Finally, Section 6 presents the conclusions.

2 SUPER TYPHOON MANGKHUT AND SST RESPONSE

A tropical depression was formed in Western Pacific on the afternoon of September 4, 2018. It then traveled westward and strengthened continuously. At 21:15 on September 7, 2018, the Japan Meteorological Agency reported the upgradation of

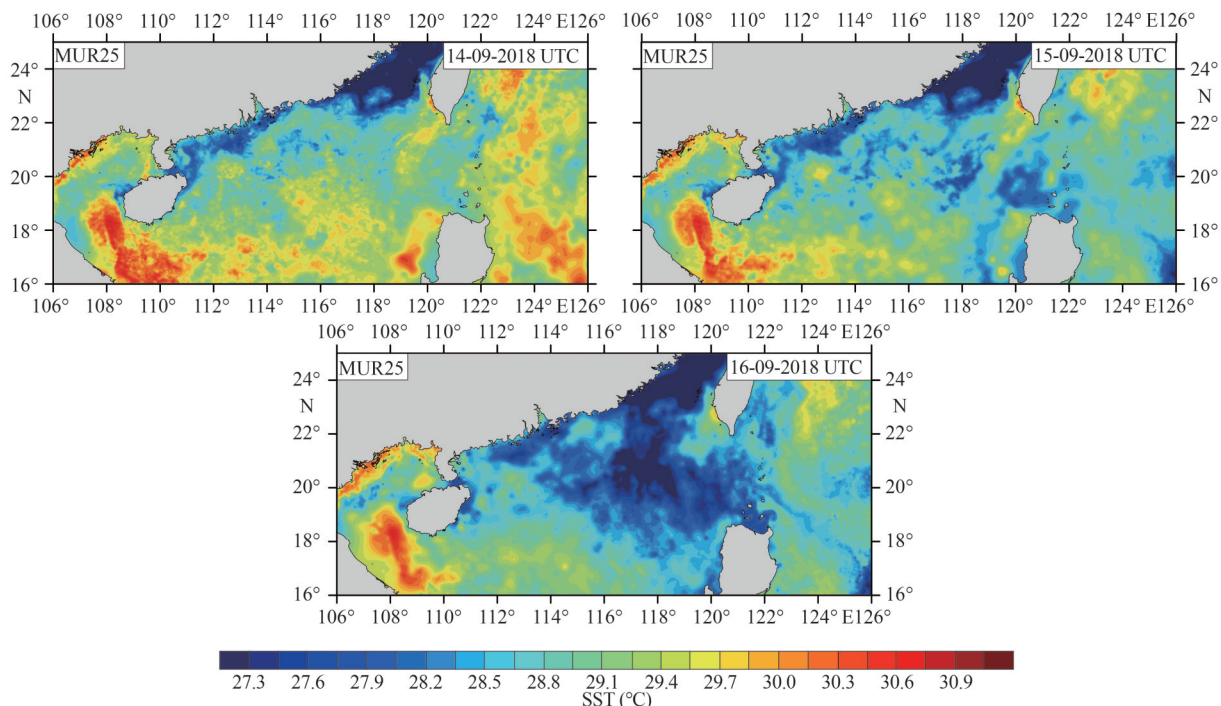


Fig.2 Spatial distribution of the sea surface temperature (SST) observed using satellite during typhoon transit

the tropical depression into a tropical storm. The phenomenon developed into a Super Typhoon on September 11, 2018, with a maximum wind speed of ~65 m/s. The typhoon caused landfall on the northeastern coast of Luzon Island in the Philippines at approximately 1:40 on September 15, 2018, with a minimum air pressure of ~910 hPa when it passed through the ARGO buoy (Fig.1a). It then entered the northeastern part of the SCS and gradually moved closer to Guangdong Province. Figure 1a shows the track of Super Typhoon Mangkhut.

Super Typhoon Mangkhut retained its intensity before causing landfall at Jiangmen. By the afternoon of September 16, 2018, it had reached the city of Jiangmen, Guangdong Province, and was rapidly decaying, with a V_{\max} of >45 m/s around the core and a P_{\min} of 955 hPa. Super Typhoon Mangkhut was the most influential and intense TC in 2018 in the North Pacific and SCS Basin, and it had a long lifespan. Additionally, it was the strongest typhoon that landed in China in 2018. Super Typhoon Mangkhut led to severe rainfall and flood flash, as well as a slew of secondary hazards, wreaking havoc on the impacted area and posing serious safety concerns.

Figure 2 shows the satellite SST serial images from the infrared and merged cloud-penetrating

microwave multiscale ultrahigh resolution (MUR) data. The MUR products have a spatial resolution of $0.01^{\circ} \times 0.01^{\circ}$ and a combination of three SST retrieval satellite datasets: the 1-km high-resolution infrared SST retrieval dataset (primarily derived from the MODIS sensor), the 4–8.8-km medium-resolution infrared SST retrieval dataset of AVHRR Global Area Coverage (GAC), and the 25-km standard sampling interval microwave SST retrieval dataset. Microwave data was used to fill the missing data caused by the interference from clouds over the SCS Basin. The data were mainly derived using the following three sensors: AMSR-E, WPR, and AMSR2. Consequently, these data can greatly reduce the influence of clouds over the SCS Basin and provide a direct observation of the SST response evolution toward Mangkhut in the SCS Basin. In the first snapshot taken on September 14, 2018, Mangkhut had not passed through the SCS Basin, and the SST was low on the SCS shelf and high in the SCS Basin. In the following snapshot taken on September 15, 2018, Mangkhut began to enter the SCS. At this time, the Luzon Strait and SCS Basin began the SST cooling; the SST was sensitive to the typhoon. In the last snapshot taken on September 16, 2018, Mangkhut crossed the SCS Basin and produced intense and widespread SST cooling over the basin.

3 MATERIAL AND METHOD

3.1 Basic data

The dataset of the observed TC best-track was produced by the Joint Typhoon Warning Center (JTWC; <http://www.usno.navy.mil/JTWC>) and China Meteorological Administration (CMA; <http://tcdatalyphoon.gov.cn>) for Super Typhoon Mangkhut, including the typhoon center, P_{\min} , and V_{\max} at 6-h intervals. The Argo data were generated from the international Argo program and the contributing national programs. For the statistics of all ARGO (<http://www.argodatamgt.org/>) data during the occurrence of Super Typhoon Mangkhut (WMO ID: 2902615; WMO ID: 2901529), the buoys closest in space and time to the typhoon center were selected for comparison. The position and observation time of buoys are presented in Table 1 and shown as red triangles in Fig.1a. The satellite data were MUR data (<https://www.ncei.noaa.gov/data/oceans/ghrsst/L4/GLOB/JPL/MUR25>), and the SST product (September 16, 2018) produced by the NASA Jet Propulsion Laboratory was used to verify the SST results obtained from the model.

3.2 Reanalysis and model data

The Hybrid Coordinate Ocean Model (HYCOM) outputs with a resolution of ~8 km were used as the initial field and boundary conditions for the CROCO model. The Final Analysis (FNL) (<http://rda.ucar.edu/datasets>) reanalysis data were used as the initial field and boundary conditions for the WRF model. The data contained information on 26 standard isobaric layers (10–100 hPa), surface boundary layer and tropopause elements. The data interval is 6 h, which means that the daily data were obtained at 00:00, 06:00, 12:00, and 18:00 h UTC. The spatial resolution of the data is $1.0^{\circ} \times 1.0^{\circ}$. The surface forcing fields of the CROCO-only model were obtained from the NCEP/NCAR reanalysis of the CFSv2 data, including wind vectors, precipitation, humidity, temperature, and atmospheric pressure.

3.3 Coupled model and its configuration

3.3.1 WRF atmospheric model

The WRF model is a non-hydrostatic, quasi-compressible weather forecasting model with static options. This model has two dynamic cores: advanced research WRF (ARW) for scientific research and non-hydrostatic mesoscale model for operational forecasting (Laprise, 1992). This model incorporates

Table 1 Coordinates and observation times at buoy points

| Buoy | Longitude (°N) | Latitude (°E) | Observation time (UTC) |
|---------|----------------|---------------|------------------------|
| 2901529 | 17.768 | 123.612 | 09-16-2018 09:20:40 |
| 2902615 | 16.808 | 122.923 | 09-15-2018 00:21:44 |

different physical processes to simulate atmospheric motion and air quality. The model has been used extensively in different fields and for studying typhoon or hurricane processes as well as air-sea interaction.

3.3.2 CROCO oceanic model

The CROCO model is an oceanic modeling system developed and maintained by France. It was built on the basis of ROMS_AGRIF and the non-hydrostatic kernel of SNH and has been gradually widely used gradually and matured (Penven et al., 2006; Debreu et al., 2012). The model solves incompressible primitive equations, similar to those in ROMS, based on the Boussinesq and hydrostatic approximations from which it inherited the robustness and efficiency of its time-splitting implementation (McWilliams et al., 2004; Shchepetkin and McWilliams, 2005; Penven et al., 2006; Uchiyama et al., 2010; Debreu et al., 2012).

3.3.3 Coupled WRF-CROCO model

The multimodel coupling platform proposed by Voldoire et al. (2017) has been extended for using the CROCO model. The CROCO-based regional coupled model was initially established by Pianezze et al. (2018) and used for simulating TCs in the southwest Indian Ocean. However, the WRF model is a mesoscale atmospheric model and has a better simulation effect than the Meso-NH model proposed by Pianezze et al. (2018) regarding the simulation of rainstorm precipitations, TCs, and mountain fires (Salgado et al., 2015; Berger et al., 2016; Bakhshaii and Johnson, 2019). Therefore, based on the framework proposed by Pianezze et al. (2018), we changed the Meso-NH model into the WRF model to build a coupled ocean-atmosphere model (WRF-CROCO).

The CROCO oceanic model was coupled to the mesoscale atmospheric model through the Ocean-Atmosphere-Sea-Ice-Soil (OASIS)-MCT, which is a coupler developed by CERFACS (Toulouse, France) to better explore the air-sea interactions and the evolution of the ocean dynamic process under the typhoon transit (Craig et al., 2017). In this study, the oceanic and atmospheric models were coupled using OASIS3-MCT_3.1. The recent version of OASIS3-MCT is interfaced with the MCT and the Spherical

Coordinate Remapping Interpolation Package (SCRIP), offering the fully parallel implementation of coupling field re-gridding and exchange (Jacob et al., 2005; Larson et al., 2005). The variables transmitted between the two models were the zonal stress, meridional stress, stress module, E-P flux, net solar flux, and net non-solar flux simulated by the atmosphere model and transferred to the ocean model via the OASIS-MCT. The SST and oceanic current calculated by the CROCO model were fed back to the atmosphere model via the OASIS-MCT. During run time, the OASIS3-MCT allowed the exchange of coupling data between the two models and interpolation and transformation of these coupling fields. The MCT was used for parallel data exchanges, and the interpolation weights were determined using SCRIP for the data transmission between the individual model grids in the MCT.

3.3.4 Model configuration

The simulation domains corresponded to the SCS and nearby regions (Fig.1b). The WRF parent and child domains were from 8°N–33°N to 99°E–133°E and from 16°N–25°N to 106°E–126°E, respectively. The CROCO simulation domain was the same as the WRF child domain for calculating computational efficiency, given that the time for the transmission of the re-gridded data among model components was reduced. The simulation time included the entire process of development and movement of Super Typhoon Mangkhut in the eastern part of the Philippines and the SCS (from 09-14-2018 06:00:00 UTC to 09-17-2018 06:00:00 UTC).

In the coupled model of Pianezze et al. (2018), the parameterization scheme of the atmospheric model Meso-NH was not comprehensive enough. The microphysical process scheme adopted the single-parameter mixed phase scheme, lacked the super-cooled water and gradual melting rate process, and disregarded the effects of land surface layer, near-surface layer, and aerosol in cloud microphysics. Therefore, for the simulation of Super Typhoon Mangkhut, WRF adopts the following physical and parameterized schemes: the recommended maximum top pressure of 5 000 Pa with a two-way nesting grid of 12 and 4 km in the horizontal direction and 30 layers in the vertical direction. The Kain-Fritsch scheme (Kain, 2004) was selected for the cumulus parameterization schemes. The long- and short-wave radiation physics were calculated based on the rapid radiative transfer mode (Mlawer et al., 1997) and the Dudhia scheme (Dudhia, 1989), respectively.

Considering that this research was conducted in the context of a super typhoon, we selected the YSU scheme (Hong et al., 2006) for the boundary layer scheme to solve the problem of inverse gradient transport caused by a large vortex transport and excessive mixing at high wind speed. The unified Noah (Chen and Dudhia, 2001) and revised MM5 Monin-Obukhov (Paulson, 1970) schemes were implemented in the land surface and surface layer schemes, respectively.

The CROCO oceanic model was covered in grid with 513×243 points in grid resolution of $1/12^\circ \times 1/12^\circ$. A total of 33 levels were used in the vertical and vertical stretching parameters $\theta_s=5.0$, $\theta_B=0.8$, $T_{\text{cline}}=150$, $V_{\text{transform}}=2$, and $V_{\text{stretching}}=4$, thus a high vertical resolution of the upper and bottom ocean layers is ensured. Eight tidal constituents (M2, S2, N2, K2, K1, O1, P1, and Q1) were applied along the open boundaries under the following conditions: the Chapman condition for the free surface, the Flather condition for 2D momentum, and the radiation plus nudging conditions for tracers and 3D momentum. The model was initialized and forced using the HYCOM output data. The third-order upstream biased advection scheme was employed to reduce the dispersion errors, and the precision of a given grid resolution was essentially enhanced (Shchepetkin and McWilliams, 1998). The nonlocal K-profile parameterization vertical turbulent mixing scheme (Large et al., 1994) was accepted to introduce a subgrid-scale vertical mixing.

The uncoupled CROCO simulation was forced using the CFSv2 data. Through the ocean-atmosphere coupled run, these data were directly provided by the WRF model in a dynamically consistent manner and updated for the SST exchange with the atmospheric model. The CROCO simulation was first run from 09-01-2018 00:00:00 UTC to 09-14-2018 06:00:00 UTC (14 d). Super Typhoon Mangkhut's simulation was performed from 09-14-2018 06:00:00 UTC to 09-17-2018 06:00:00 UTC, for a total of 72 h. In the CROCO and WRF simulation, the timesteps were set to 60 s, and the time step of the OASIS3-MCT was set to 120 s to coordinate the variable transferred between the models.

4 MODEL VALIDATION

4.1 Typhoon track

Figure 3a displays the comparisons between the track of Super Typhoon Mangkhut in two simulation experiments (red and blue lines in Fig.3a) and the

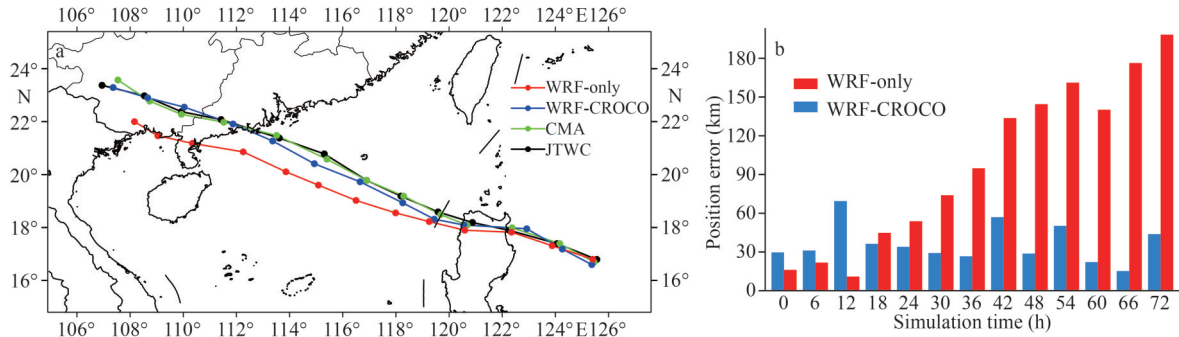


Fig.3 Simulated and observed track of Super Typhoon Mangkhut (a) and the track deviation between the Joint Typhoon Warning Center (JTWC) and the two simulation experiments (b)

Map review No. GS(2022)4318.

two observed tracks, with one using the CMA (green line in Fig.3a) data and the other using the data generated by the JTWC (black line in Fig.3a). The two simulated tracks generally followed the two observed tracks closely except when the storm caused a landfall at the Chinese local time 12:00:00 on September 16, 2018. The moving speed of the typhoon in the simulations of the WRF-only experiment was slower than that in the WRF-CROCO experiment, but this was not particularly evident. Figure 3b shows the track deviation between the JTWC and the two simulation experiments. As shown in the figure, the WRF-only experiment track error gradually increased as the typhoon moved, especially after 36 h. The moving speed of WRF-CROCO simulation results can better keep up with the JTWC in the SCS; the error change was relatively stable and controlled within a range of 60 km, which was smaller than the WRF-only experiment. Through the above results, it can be concluded that the simulation results of Super Typhoon Mangkhut in the WRF-CROCO experiment were somewhat consistent with the actual observations in the SCS.

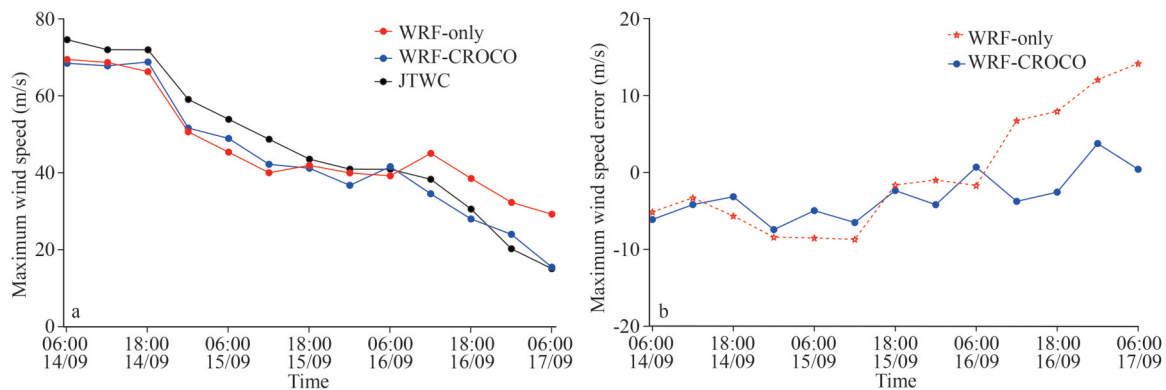


Fig.4 Simulated and observed maximum wind speed of Super Typhoon Mangkhut (a) and the maximum wind speed deviation between the Joint Typhoon Warning Center (JTWC) and the two simulation experiments (b)

4.2 Typhoon intensity

The time series of the simulated maximum wind speed from the two simulation experiments were compared with the observations from JTWC (Fig.4a). The maximum wind speed trends of the two simulation experiments were consistent with the observations from JTWC. Compared with the observed maximum wind speed of Super Typhoon Mangkhut, coupled WRF-CROCO case (blue line) showed better simulation performance than the WRF-only case (red line) in the SCS. Especially during the landfall, the deviation of the WRF-only case exceeded 10 m/s, whereas that of the coupled WRF-CROCO case was relatively small (Fig.4b). In the coupled simulation, SST was calculated from the ocean model into the atmospheric model for a real-time impact, which then slightly adjusted the track of Super Typhoon Mangkhut and improved the problem of the maximum wind speed simulation in the WRF model.

Figure 5a shows the comparison between the observed and simulated minimum sea level pressure (SLP_{min}). The figure reveals that the two simulation

experiments performed well in general compared with the observations from JTWC throughout the whole simulation period. Although these experiments can reproduce its changes, all the experiments underestimated SLP_{min} when Super Typhoon Mangkhut passed over the Philippines (00:00, September 15, 2018) and entered the SCS (06:00, September 15, 2018). The SLP_{min} trend gradually rose, which means that the intensity of Super Typhoon Mangkhut gradually weakened during the second landfall in China.

Figure 5b shows the deviation between the observed SLP_{min} from JTWC and the simulation results. The figure indicates that the difference between the simulated and observed values was negative after 30 h, demonstrating that the simulated result was underestimated for the observed SLP_{min} . Thus, the simulation intensity was overestimated for the actual intensity in the SCS.

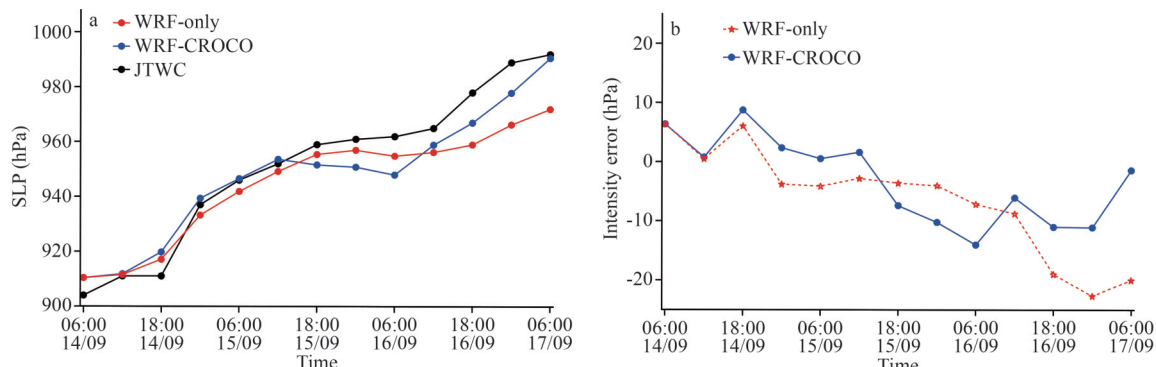


Fig.5 Simulated and observed minimum sea level pressure (SLP_{min}) of Super Typhoon Mangkhut (a) and the minimum sea level pressure (SLP_{min}) deviation (simulation value minus observation value) between the Joint Typhoon Warning Center (JTWC) and the two simulation experiments (b)

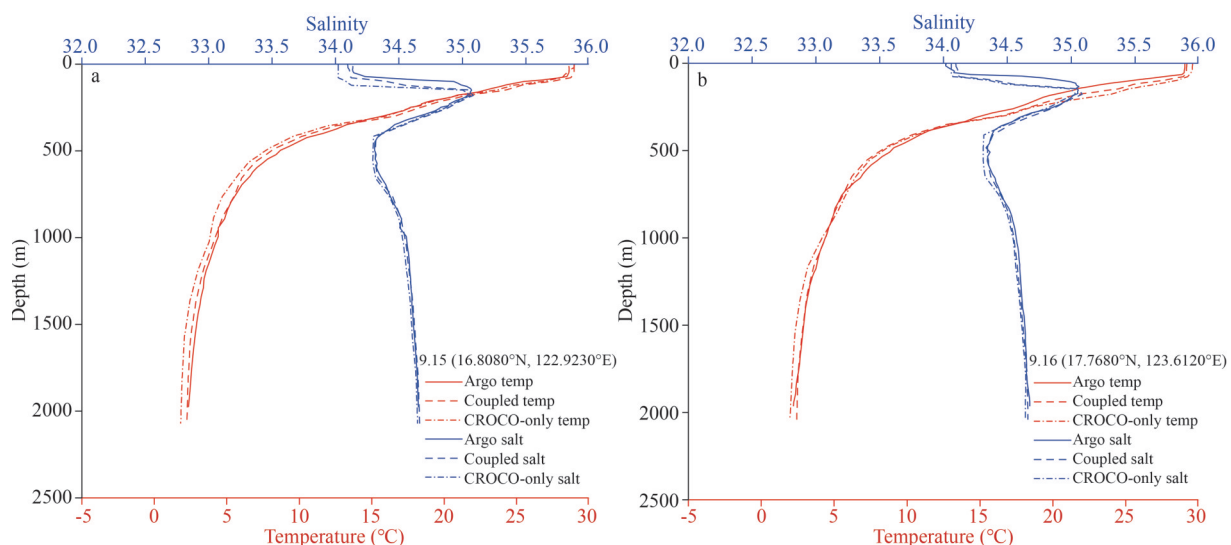


Fig.6 Comparison of temperature and salinity between simulated (a) and Argo (b)

4.3 Ocean temperature and salinity

The Argo database was used to collect the buoys' data in the simulated sea region during the typhoon, and the temperature and salinity profile data of the upper ocean layer were compared with those from the model simulation. There were two Argo observational buoys, one (WMO ID: 2902615) on the left side of Mangkhut and the other (WMO ID: 2901529) on the right (Fig.1a). Figure 6 shows that the temperature and salinity distribution of the two cases exhibit good fitting with the results of the Argo dataset and are distributed near the dataset, reflecting the consistency between the simulation and measured results. In these two contrast positions, a slight difference was observed between the results of WRF-CROCO and WRF-only cases and the vertical profiles almost coincided. The simulation effect of the WRF-CROCO case was better than that of the WRF-

only case, but the difference was insignificant. The SST measured by buoy 2902615 was approximately 0.6 °C below the simulated result, whereas the salinity was greater than the simulated result at approximately 1.2. The SST measured by buoy 2901529 was approximately 0.5 °C below the simulated result, whereas the salinity was greater than the simulated result of ~1.0. Therefore, the vertical profiles of ocean temperature and salinity should be reasonable in the simulation of Super Typhoon Mangkhut.

Comparing the results of the WRF-CROCO model, the WRF-only experiment, and the observations, the variation trend of the intensity deviation differed under the two experimental scenarios. The simulation deviation slightly increased in the middle and late stage of the simulation; however, the deviation between the coupled case (WRF-CROCO) simulated result of V_{max} and the observations from JTWC was within the range of 10 m/s and the deviation in SLP was controlled within the range of 15 hPa in the SCS. The coupled case (WRF-CROCO) simulation performed better than the single case (WRF-only) and can simulate the strength and intensity of Super Typhoon Mangkhut and the vertical temperature and salinity distribution of the ocean. Evidently, the coupled case (WRF-CROCO) simulation results accurately present the evolution of the thermal and dynamic processes of the typhoon in the SCS.

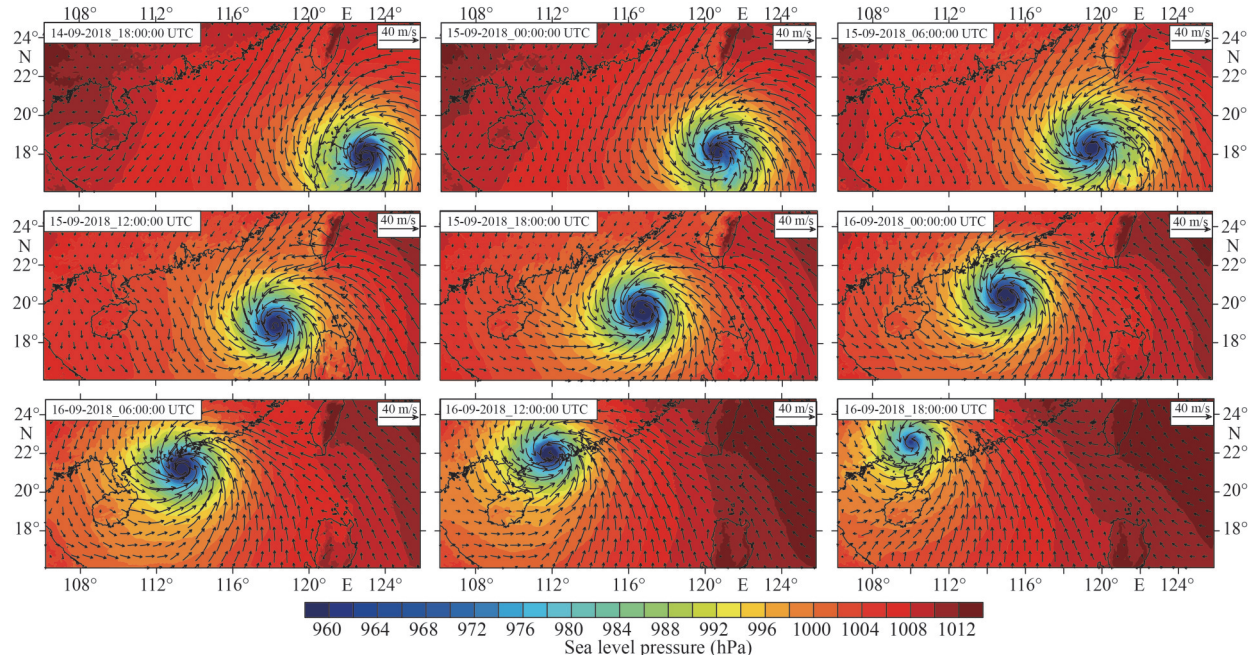


Fig.7 Spatial distribution for simulated wind and pressure fields

5 RESULT AND DISCUSSION

5.1 Typhoon response to the ocean

5.1.1 Wind and pressure field

Figure 7 clearly displays the spatial distribution of the V_{10} and SLP simulated in the WRF-CROCO experiment. The process of the change in wind and pressure fields of Super Typhoon Mangkhut intuitively moved from the northwest of the Philippines to the SCS until it landed in China. When Super Typhoon Mangkhut passed through the Philippines and reached the SCS, the wind field of the typhoon considerably decreased, especially after the typhoon landed in the Philippines at 18:00:00 UTC on September 14, 2018, with a sustained wind velocity of >40 m/s. The wind field strength of the typhoon rapidly declined after landing in Guangdong Province. Given the effect of Coriolis force, the region of high wind speed appeared on the right side of the typhoon center. Similar to the wind field, the pressure increased strongly when it caused landfall over the Philippines at 18:00:00 UTC on September 14, 2018. As it reached the SCS Basin and gradually moved northwest, the SLP was maintained at >950 hPa and rapidly decayed after the landfall. The center of the V_{10} was approximate to the center of the SLP, and the pressure field was symmetrical along the track of Super Typhoon Mangkhut. The high-value

region of the pressure gradient appeared on the right side of the track.

The shear stress at the sea-air interface affects the near-surface ocean currents, and the wind stress under the influence of Super Typhoon Mangkhut is of great significance to exploring its sea-air interaction process. Figure 8 shows the spatial distribution of the wind stress zonal component and the meridional component of Super Typhoon Mangkhut in the SCS Basin. At 08:00 UTC on September 15, 2018, the surface u - and v -momentum stresses were approximately 3.5 and 5 N/m², respectively. During the movement to the northwest, the typhoon's intensity weakened, and the corresponding wind stress showed a considerable change. At 22:00 UTC on September 15, 2018, the zonal surface stress decreased to ≤ 2 N/m², and the meridional stress decreased to ~ 3.5 N/m². The surface meridional wind stress was slightly greater than the surface zonal wind stress.

5.1.2 Heat flux

As an important energy source for typhoon maintenance and development, the heat flux is the main transmission method in heat exchange. The spatial distribution of the latent heat flux (Fig.9) displays that the latent heat flux decreased greatly as the typhoon weakened during its movement toward the northwest. The region with the latent heat flux extremum appeared in the helical flux area near the typhoon center. The maximum value of the latent

heat flux was 800 W/m² after the typhoon reached the SCS Basin at 12:00 UTC on September 15, 2018. When the typhoon landed at 12:00 UTC on September 16, 2018, the latent heat flux in most areas decreased to ~ 700 W/m², except the coastal area.

Under the same conditions during Super Typhoon Mangkhut, the sensible heat flux (Fig.10) shows that the region with the sensible heat flux extremum appeared in the helical flux area near the typhoon center with a positive value in the SCS Basin, which can reach ~ 180 W/m².

From the simulation performance of the latent and sensible heat fluxes during the Super Typhoon Mangkhut process, latent heat played a substantial role in changing the heat flux dramatically during Super Typhoon Mangkhut in the SCS basin. Therefore, reduction in the SST is the most direct influence of heat transfer caused by sea surface evaporation during a typhoon.

To further explore the results of heat flux under the influence of Super Typhoon Mangkhut in the SCS Basin and shelf, we compared the radial distribution of azimuth mean SST, heat flux, SLP, and 10-m wind speed from 03:00 UTC to 06:00 UTC on September 16, 2018, via a coupling simulation (Fig.11). The atmosphere received less energy when the SST was low, resulting in low pressure and wind fields. The azimuth mean radial distribution of the 10-m wind speed was similar to the heat flux

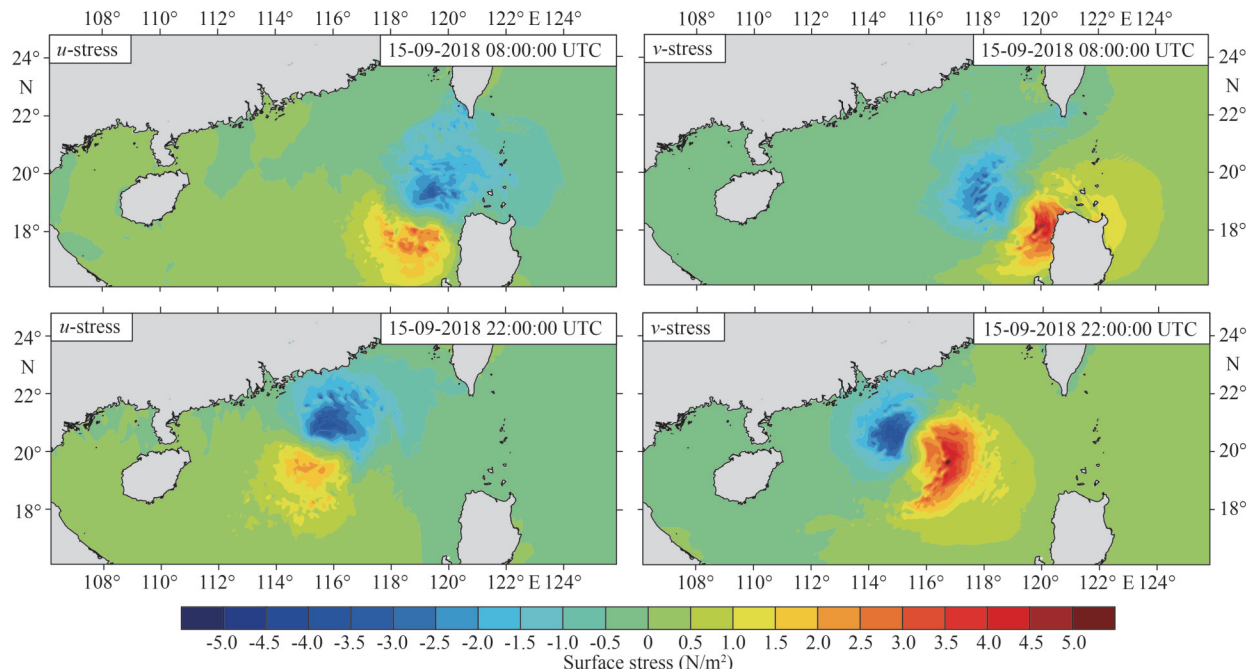


Fig.8 Spatial distribution for simulated surface stress

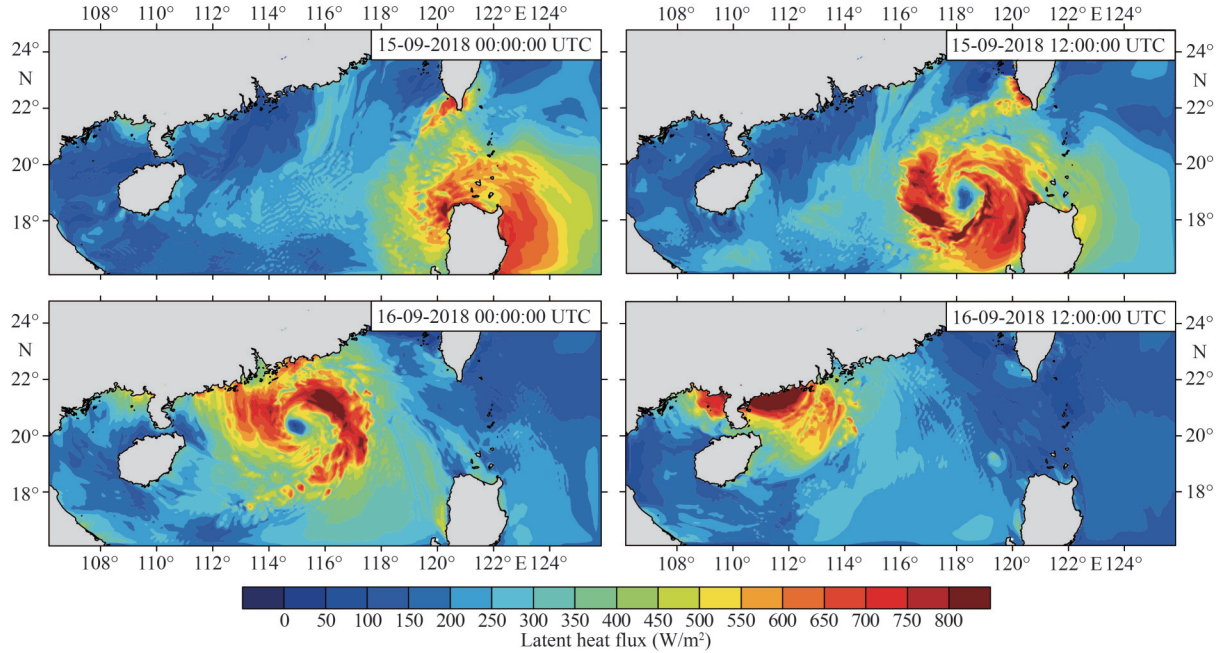


Fig.9 Spatial distribution for simulated latent heat flux

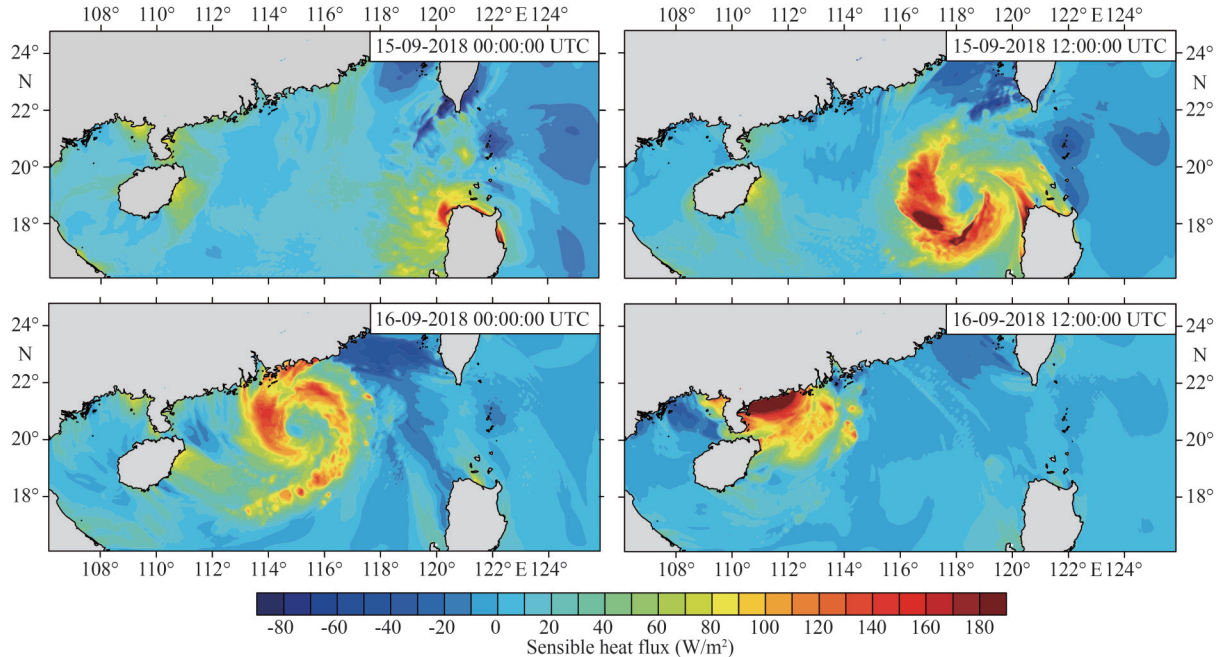


Fig.10 Spatial distribution for simulated sensible heat flux

distribution, but the heat flux was more sensitive to the SST. According to the definition given by Weatherford and Gray (1988), the region between the typhoon center and 111 km from the typhoon center is the typhoon inner-core region, and the region between 111 and 278 km from the typhoon center is the periphery region. The difference in the heat flux was mainly observed in the inner-core region, especially at the position of the maximum

wind speed radius. Table 2 presents the changes in average wet enthalpy, SST, and minimum sea level pressure beneath the inner-core region of the typhoon between 03:00 UTC and 09:00 UTC in the SCS Basin. Table 3 shows the difference between the average wet enthalpy, SST, and minimum sea level pressure at the simulation times. The variation in the SST below the typhoon's inner-core region greatly affects the heat flux exchange, whereas the

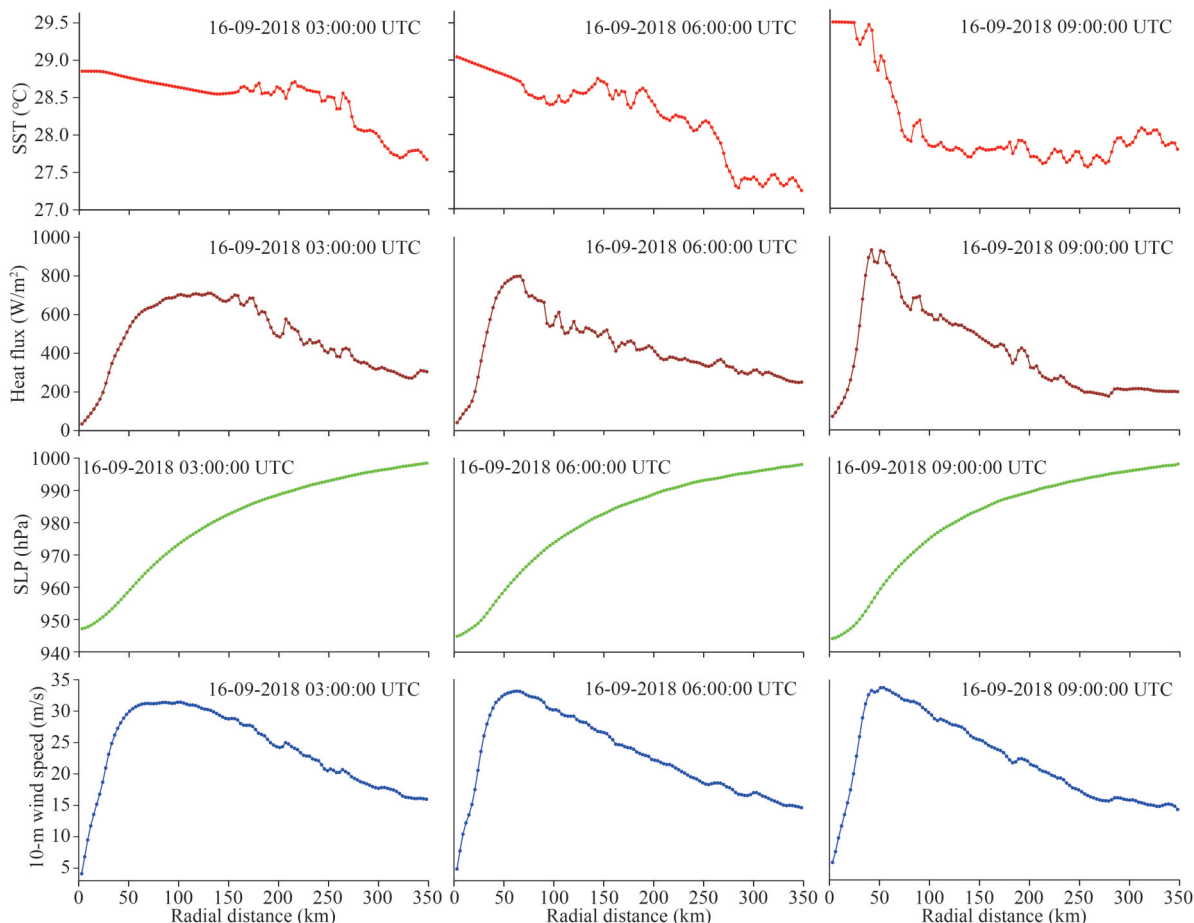


Fig.11 Radial distribution of azimuth mean SST, heat flux, sea surface pressure (SLP), and 10-m wind speed at 03:00 UTC, 06:00 UTC, and 09:00 UTC on September 16, 2018

Table 2 Average wet enthalpy, sea surface temperature (SST), and minimum sea level pressure (SLP_{min}) beneath the inner-core region of the typhoon between 03:00 UTC and 09:00 UTC on September 16, 2018

| Simulation time (UTC) | Wet enthalpy (W/m ²) | SST (°C) | SLP _{min} (hPa) |
|-----------------------|----------------------------------|----------|--------------------------|
| 09-16-2018 03:00:00 | 452.73 | 28.72 | 947.9 |
| 09-16-2018 06:00:00 | 473.15 | 28.84 | 945.8 |
| 09-16-2018 09:00:00 | 533.93 | 29.13 | 944.1 |

Table 3 Average Wet enthalpy ratio, sea surface temperature (SST), and minimum sea level pressure (SLP_{min}) difference beneath the inner-core region of the typhoon between 03:00 UTC and 09:00 UTC on September 16, 2018

| Simulation time (UTC) | Wet enthalpy ratio (%) | SST (°C) | SLP _{min} (hPa) |
|------------------------------|------------------------|----------|--------------------------|
| 09-16-2018 03:00:00–06:00:00 | 4.51% | 0.12 | 2.1 |
| 09-16-2018 06:00:00–09:00:00 | 12.84% | 0.29 | 1.7 |
| 09-16-2018 03:00:00–09:00:00 | 17.94% | 0.41 | 3.8 |

decrease in the SST below the typhoon's inner-core region results in a decrease in heat flux exchange. The average SST on the SCS Basin at 03:00 UTC was 0.12 °C lower than that at 06:00 UTC; the wet enthalpy (latent heat+sensible heat) was reduced by 4.51%, and the central pressure increased by 2.1 hPa. Compared with 09:00 UTC in the SCS shelf, the average SST of 06:00 UTC in the SCS Basin decreased by 0.29 °C, the wet enthalpy decreased by 12.84%, and the central pressure increased by 1.7 hPa. Compared with 09:00 UTC, the average SST of 03:00 UTC decreased by 0.41 °C, the wet enthalpy decreased by 17.94%, and the central pressure increased by 3.8 hPa. The variation in the SST below the typhoon's inner-core region greatly affects the heat flux exchange between the ocean and atmosphere, whereas the decrease in the SST below the typhoon's inner-core region results in a decrease in heat flux exchange. The SST below the inner-core region cooled by 1 °C, resulting in a 37%–44%

decrease in wet enthalpy, and the central pressure increased by approximately 9 hPa in the SCS Basin.

5.1.3 Equivalent potential temperature

The equivalent potential temperature can be written as $\theta_e = \theta \exp \frac{L_v q_s}{c_p T}$, where $\theta = T \left(\frac{1000}{P} \right)^{\frac{R}{c_p}}$ is the potential temperature, c_p is the constant-pressure specific heat capacity, T is the temperature, L_v is the latent heat of phase change, q_s is the saturation specific humidity, and R is the specific gas constant. The distribution of equivalent potential temperature can represent the distribution of moist static energy (moist static energy $\Phi_m = c_p T + g_z + L_q$, which is the sum of apparent, potential, and latent heat energies). Figure 12 shows that the radial distribution of the potential equivalent temperature at three different times varied in the inner-core region of the typhoon. At a distance 30 m away from the center of the typhoon, the potential equivalent temperature was 374.71 K at 03:00 UTC, 376.23 K at 06:00, and 376.53 K at 09:00 on September 16, 2018. The potential equivalent temperature differences between the typhoon center and 111 km from the typhoon center were 15.03 K at 03:00 UTC, 18.12 K at 06:00 UTC, and 19.46 K at 09:00 on September 16, 2018, respectively. Based on the sea surface pressure presented in Fig.11 (third panel), the greater the radial gradient of the equivalent potential temperature, the stronger the typhoon intensity.

5.2 Ocean response to the typhoon

5.2.1 Flow field

A strong corresponding relationship exists between wind and current; that is, strong wind stress leads to a strong ocean current. When a typhoon passes, it forms a strong rotating wind field accompanied by a distinct wind-induced current. As shown in Fig.13, given the impact of Super Typhoon Mangkhut, the

wind-induced current in the SCS Basin has changed considerably. The strong winds correspond to a high current speed, which appears on the right side of the typhoon's center, with a maximum current speed of 2.5 m/s. At this time, the flow field presented an obvious asymmetrical distribution in the surface layer. Although the time interval was 3 h, good correspondence remained between the wind and current on the right side of the typhoon; that is, the strong wind produced a strong current. The center of the flow field was located right behind the typhoon's center, and the maximum flow velocity was located on the right side of the typhoon center. Thus, the center of the flow field has a small lag relative to the center of the wind field.

5.2.2 SST

Under the influence of typhoons, the SST will decrease considerably. This section mainly explores the variation in the SST from the perspective of model simulation performance evaluation. The spatial distribution of the SST (Fig.14) shows that all three charts reflect the sea surface cooling caused by the typhoon. In the first column, the temperature field distribution of the CROCO-only case shows that the cooling range and area are relatively small compared with the coupled case (column 2) and MUR25 data (column 3). In the second column, WRF-CROCO was used, and it was closest to the MUR25 dataset in terms of morphological distribution and cooling amplitude. Therefore, in this paper, the coupled case was found to be better than the uncoupled case for simulating the SST decrease caused by Super Typhoon Mangkhut in the SCS Basin. Figure 15 displays the variation distribution of the SST, with the reference time of 06:00:00 on September 14, 2018. The SST in the SCS changed slightly. At 18:00 UTC on September 14, 2018, before the typhoon passed, the SST cooling began in

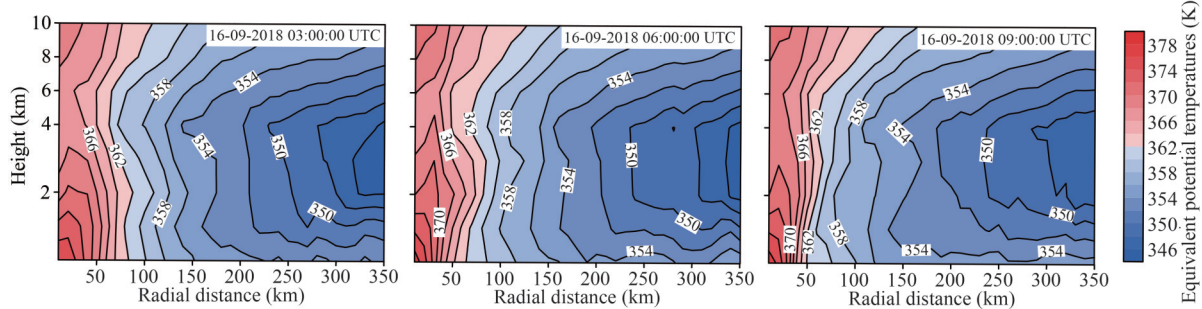


Fig.12 Radial distribution of azimuth mean equivalent potential temperatures at 03:00 UTC, 06:00 UTC, and 09:00 UTC on September 16, 2018

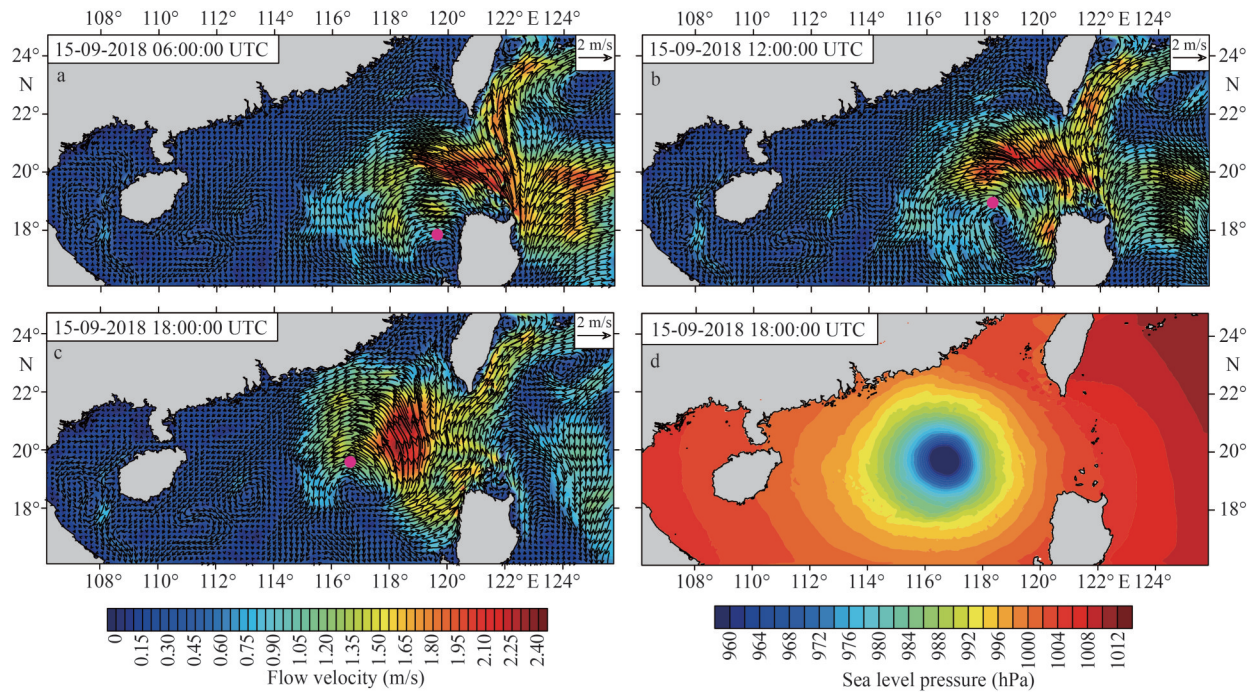


Fig.13 Spatial distribution for simulated flow field

The flow field is drawn with an arrow; the flow speed (unit: m/s) corresponds to the background colors in (a)–(c); the SLP (unit: hPa) corresponds to the background color in (d). The pink dots represent the center of the typhoon.

the northeastern Philippines. At 00:00 UTC on September 15, 2018, in the SCS Basin, given the influence of Super Typhoon Mangkhut, the SST near the typhoon center markedly showed cooling, and the maximum SST cooling was approximately 4 °C.

Similar to the flow field, the SST presented an evident asymmetric spatial distribution along the track. The SST with a strong cooling region appeared on the right side of the typhoon path in the SCS, regardless of the range or magnitude of the

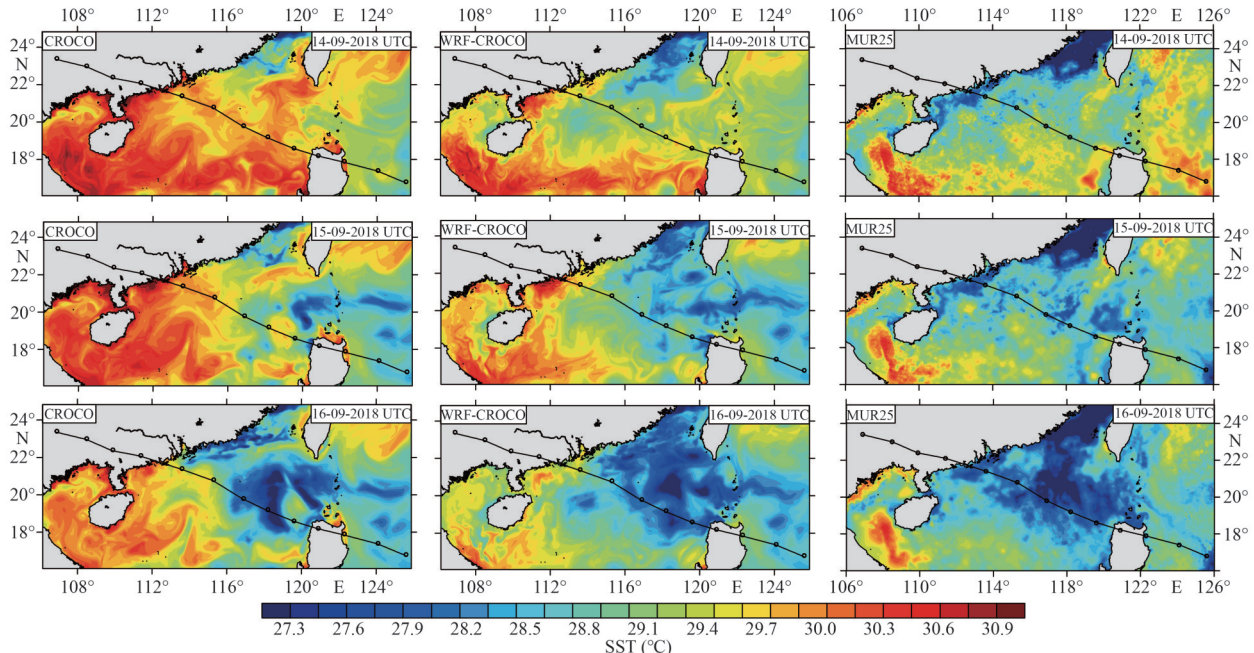


Fig.14 Spatial distribution for the simulated and satellite observed sea surface temperature (SST) during typhoon transit

Black line represents the typhoon track.

temperature drop. The SST cooling on the left side of the typhoon path was approximately 2.5°C , while that on the right side was more than 4°C in the SCS Basin, owing to the resonance of the near-inertial oscillation, with the wind vector rotating clockwise locally as the typhoon passed.

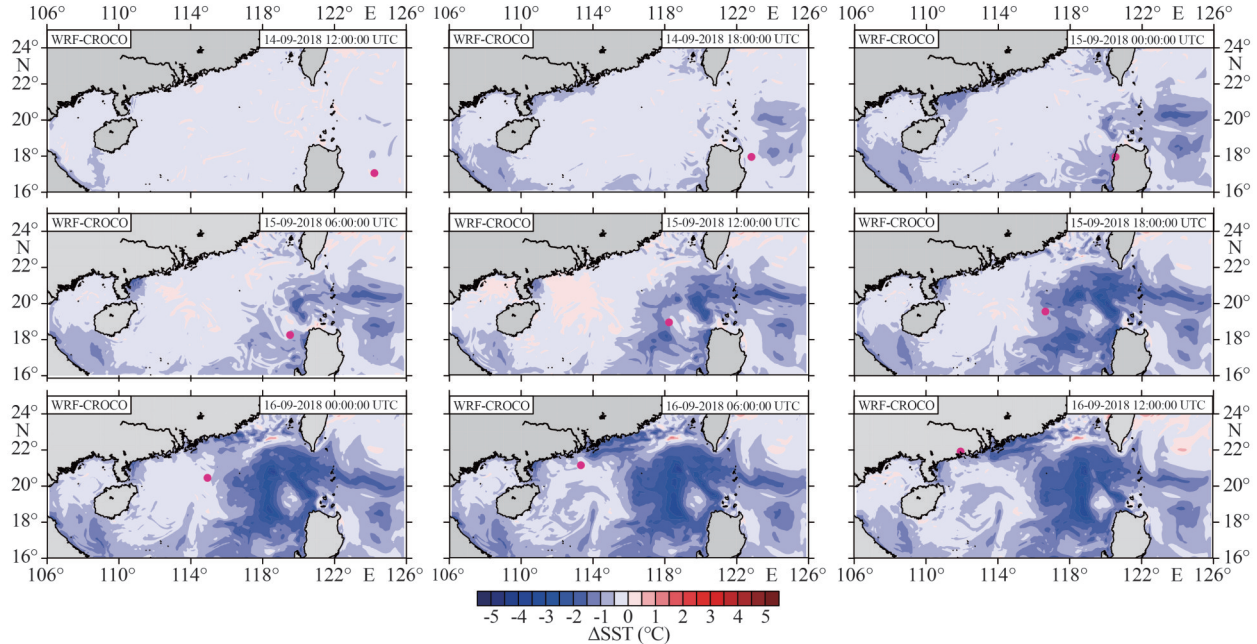


Fig.15 Spatial distribution of the deviation between sea surface temperature (SST) and initial sea surface temperature (SST) (reference time: 09-14-2018 06:00:00 UTC) during typhoon transit

Black line represents the typhoon track; time interval: 3 h. The pink dots represent the center of the typhoon.

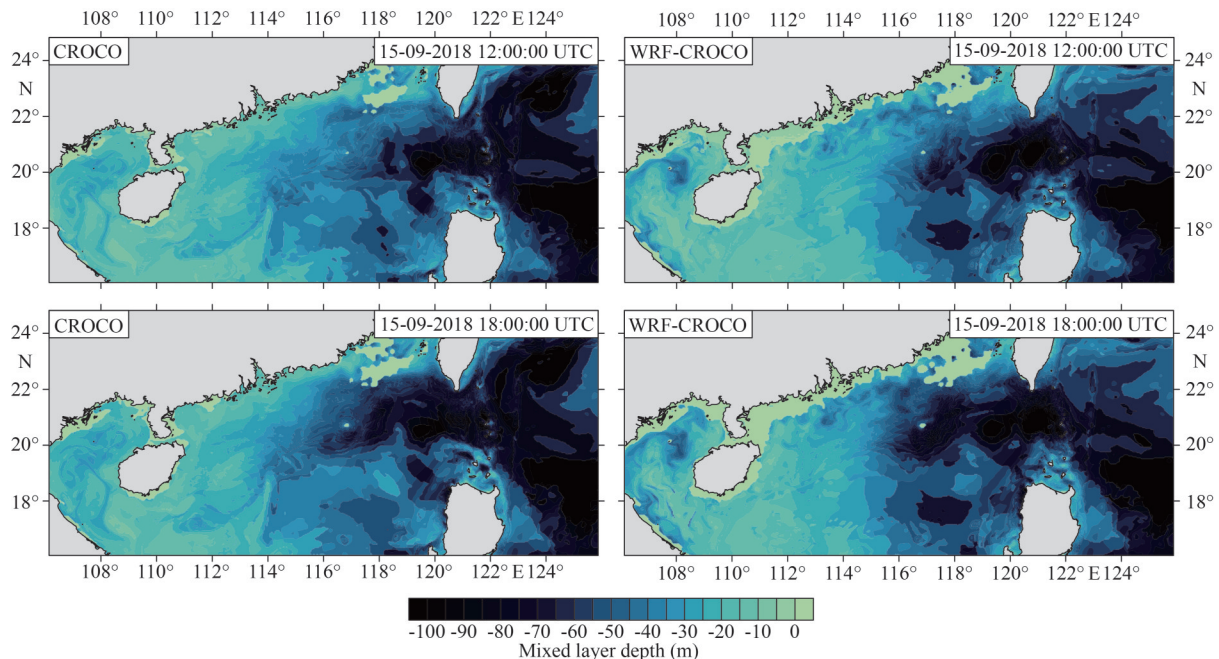


Fig.16 Spatial distribution of simulated mixing layer depth during typhoon transit

Images on the left side show the results obtained in the CROCO-only case, and images on the right side present the observations in the WRF-CROCO case.

5.2.3 Oceanic boundary layer (OBL)

To explain the drop in SST during the typhoon in the SCS Basin (Fig.15), we considered the evolution of the OBL. The depth of the marine ML will change substantially during the typhoon. Figure 16 shows that the ML depth obtained via the CROCO-

only experiment was affected by astronomical tidal forcing, while that obtained by the WRF-CROCO experiment was affected by the real-time sea-air interaction, found using the sea-air coupling model.

As shown in Fig.16, the spatial distribution of the ML depth, which was affected by the astronomical tidal force in the CROCO-only experiment, was stable at different times. Given the influence of nearshore tide and coastal circulation, the ML depth reached ~ 10 m. Near the deep basin northeast of the SCS, the ML depth reached 60 m due to the large depth of ocean. When the typhoon reached the SCS and moved northwest at 18:00 UTC on September 15, 2018, the ML deepened, reaching a maximum of ~ 80 m.

To further explain the SST cooling phenomenon in the typhoon process in the SCS Basin, we examined the time evolution of thermocline and ocean current. Vertical profiles were extracted at point (A), as shown by the red star in Fig.17a. This point, which highlights the response of thermocline

after the transit of Mangkhut, is located in the strongest cooling region of the SST during Super Typhoon Mangkhut in the SCS Basin. Figure 17 shows the temporal evolution of the vertical profiles of the oceanic temperature, temperature vertical diffusion coefficient, mean SLP (MSLP), and currents obtained at this point. Figure 17b shows that in the first 21 h, the SST remains at 29°C and the observed thermocline appears at a 40–45-m depth. During the 15–25 h of simulation, the SST decreased from 29°C to $<26^{\circ}\text{C}$ as the typhoon approached and passed point A (where the MSLP was minimum, as shown in Fig.17d). Notably, the maximum cooling of SST occurred for more than 6 h after the typhoon had passed. At 35 h of simulation, which was 3 h after the typhoon, the thermocline dropped to a depth of 110 m. When the typhoon arrived near point A, the temperature vertical diffusion coefficient (Fig.17c) increased sharply to $0.26\text{ m}^2/\text{s}$ at 32 h of simulation. Thus, the temperature was considerably declined by the vertical exchange under the influence of the typhoon,

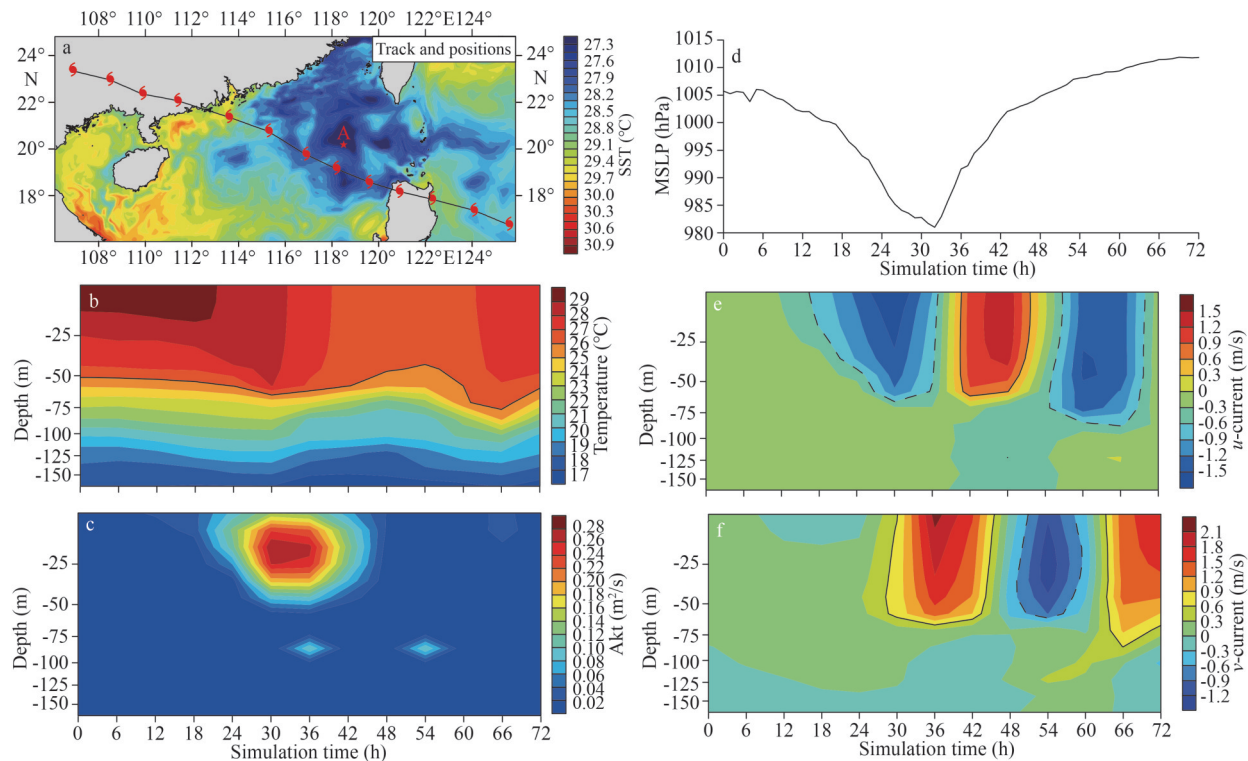


Fig.17 Spatial distribution for simulated sea surface temperature (SST) on September 16, 2018 (a); time series of the vertical profiles of oceanic temperature (b); the temperature vertical diffusion coefficient Akt (c) and the mean sea level pressure (MSLP) (d); the u - (e) and v - (f) components of the oceanic current

The red star on (a) (point A) denotes the location of the vertical profiles of temperature and currents. The black isoline in (b) represents the 26°C isotherm. The -0.6 and 0.6 m/s isolines in (e) & (f) are drawn using the dashed and solid contours, respectively. All these variables were obtained from point A ($118.5^{\circ}\text{E}, 20.2^{\circ}\text{N}$) with a red star.

and it can be used to explain that the depth increase of the OBL was primarily due to vertical mixing.

Figure 17e–f shows that as Super Typhoon Mangkhut approached point A, the u -component of the oceanic current gradually presented a large negative value (east-west direction) after 15 h of simulation and increased from -0.6 to -1.4 m/s. The maximum negative value was reached after 30 h of simulation and 2 h before the typhoon approached point A. After 40 h of simulation, the typhoon had passed, and with the departure of the typhoon center and movement of the wind field, the meridional flow became positive (west-east direction) and reached a maximum value of 1.4 m/s in the 50th hour of simulation and turned negative again in the 57th hour of simulation; that is, 25 h after the typhoon passed. The v -component of the oceanic current also changed substantially with the arrival of the typhoon. After 32 h of simulation, that is, when the typhoon approached point A, it showed a significant positive value (south-north direction) and increased from 0.3 m/s to a maximum value of 2.1 m/s between the surface and 55-m depth. After 48 h of simulation, two-direction changes were observed. An inertial oscillation of the oceanic current with a period of 1 d was observed between 0- and 75-m in depth in the SCS basin. A strong inertial current up to ~2.28 m/s was induced by Super Typhoon Mangkhut in the upper ocean. The v -component of the oceanic current relatively lagged behind the u -component over time due to the Mangkhut moving from southeast to northwest.

6 CONCLUSION

In this study, the atmospheric and oceanic responses to Super Typhoon Mangkhut in the SCS Basin were investigated based on satellite SST data and numerical simulation. Mangkhut approached and caused landfall in the Philippines on September 15, 2018, and then caused landfall in Guangdong Province, China, on September 16, 2018. The infrared (MODIS, GAC) and merged cloud-penetrating microwave MUR data indicated that the Super Typhoon Mangkhut resulted in a strong SST response in the SCS Basin. When compared with CROCO-only, the coupled ocean-atmosphere model (WRF-CROCO) can accurately simulate the evolution of the thermal and dynamic processes of the typhoon in the SCS Basin.

According to the spatial distribution of wind and flow fields, the influences of Coriolis force, the V_{10} ,

SLP, and ocean current on the right side of the typhoon's center were notably greater than those on the left side. Similar to the flow field, the SST presented an evident asymmetrical spatial distribution along the path in the SCS Basin. This can be explained in the analysis of the ocean boundary layer. We found that the maximum cooling region in the SCS Basin, to the right side of the typhoon's track, produced an inertial oscillation of the oceanic current with a period of 1 d at 0–75-m depth and a strong inertial current up to ~2.28 m/s in the upper ocean. The inertial oscillation resonates with the locally clockwise rotating wind and flow field on the right side, enhancing turbulent mixing in the region and inducing a strong SST cooling. Moreover, when the SST was low, the energy obtained by the atmosphere was low, resulting in weak wind and pressure fields. The azimuth mean radial distribution of the wind speed was consistent with the heat flux distribution in the SCS Basin, but the sensitivity to the SST was different; heat flux was more sensitive than wind speed.

The wet enthalpy distribution in the SCS Basin's typhoon inner-core region responded significantly to the underlying SST of the typhoon. The SST below the inner-core region was cooled by 1 °C, resulting in a 37%–44% decrease in wet enthalpy, and the central pressure was increased by ~9 hPa. The present study emphasizes that the changes in SST below the inner-core region of the SCS Basin have a significant impact on air-sea fluxes under high-wind conditions.

The storm-induced cooling of the sea surface in the SCS Basin lowered the amount of wet enthalpy transported from the ocean to the atmosphere, lowering the moist static energy in the typhoon boundary layer. The analysis of equivalent potential temperature, which represents the moist static energy, shows that the decrease in the equivalent potential temperature and its gradient weakened the typhoon intensity, and good correspondence between the difference in equivalent potential temperature (moist static energy) and the typhoon intensity was observed, indicating that the influence of wet enthalpy on typhoon intensity cannot be overlooked.

7 DATA AVAILABILITY STATEMENT

The datasets generated and/or analyzed for the current study are available from the corresponding author.

8 ACKNOWLEDGMENT

The authors thank Jiuwei ZHAO, Nanjing University of Information Science and Technology, for providing guidance, and acknowledge the High Performance Computing Center of Nanjing University of Information Science and Technology for their support to this work.

References

- Bakhshai A, Johnson E A. 2019. A review of a new generation of wildfire-atmosphere modeling. *Canadian Journal of Forest Research*, **49**(6): 565-574, <https://doi.org/10.1139/cjfr-2018-0138>.
- Bender M A, Ginis I. 2000. Real-case simulations of hurricane-ocean interaction using a high-resolution coupled model: effects on hurricane intensity. *Monthly Weather Review*, **128**(4): 917-946, [https://doi.org/10.1175/1520-0493\(2000\)128<0917:RCSOHO>2.0.CO;2](https://doi.org/10.1175/1520-0493(2000)128<0917:RCSOHO>2.0.CO;2).
- Bender M A, Ginis I, Tuleya R et al. 2007. The operational GFDL coupled hurricane-ocean prediction system and a summary of its performance. *Monthly Weather Review*, **135**(12): 3965-3989, <https://doi.org/10.1175/2007MWR2032.1>.
- Berger A, Barbet C, Leriche M et al. 2016. Evaluation of Meso-NH and WRF/CHEM simulated gas and aerosol chemistry over Europe based on hourly observations. *Atmospheric Research*, **176-177**: 43-63, <https://doi.org/10.1016/j.atmosres.2016.02.006>.
- Black W J, Dickey T D. 2008. Observations and analyses of upper ocean responses to tropical storms and hurricanes in the vicinity of Bermuda. *Journal of Geophysical Research*, **113**(C8): C08009, <https://doi.org/10.1029/2007JC004358>.
- Chen F, Dudhia J. 2001. Coupling an advanced land surface-hydrology model with the Penn State-NCAR MM5 modeling system. Part I: model implementation and sensitivity. *Monthly Weather Review*, **129**(4): 569-585, [https://doi.org/10.1175/1520-0493\(2001\)129<0569:CAALSH>2.0.CO;2](https://doi.org/10.1175/1520-0493(2001)129<0569:CAALSH>2.0.CO;2).
- Chen G X, Xue H J, Wang D X et al. 2013. Observed near-inertial kinetic energy in the northwestern South China Sea. *Journal of Geophysical Research*, **118**(10): 4965-4977, <https://doi.org/10.1002/jgrc.20371>.
- Chen S S, Price J F, Zhao W et al. 2007. The CBLAST-hurricane program and the next-generation fully coupled atmosphere-wave-ocean models for hurricane research and prediction. *Bulletin of the American Meteorological Society*, **88**(3): 311-313, <https://doi.org/10.1175/BAMS-88-3-311>.
- Chiang T L, Wu C R, Oey L Y. 2011. Typhoon Kai-Tak: an ocean's perfect storm. *Journal of Physical Oceanography*, **41**(1): 221-233, <https://doi.org/10.1175/2010JPO4518.1>.
- Chu P C, Veneziano J M, Fan C W et al. 2000. Response of the South China Sea to tropical cyclone Ernie 1996. *Journal of Geophysical Research*, **105**(C6): 13991-14009, <https://doi.org/10.1029/2000JC900035>.
- Cione J J, Uhlhorn E W. 2003. Sea surface temperature variability in hurricanes: implications with respect to intensity change. *Monthly Weather Review*, **131**(8): 1783-1796, <https://doi.org/10.1175//2562.1>.
- Craig A, Valcke S, Coquart L. 2017. Development and performance of a new version of the OASIS coupler, OASIS3-MCT_3.0. *Geoscientific Model Development*, **10**(9): 3297-3308, <https://doi.org/10.5194/gmd-10-3297-2017>.
- Debreu L, Marchesiello P, Penven P et al. 2012. Two-way nesting in split-explicit ocean models: algorithms, implementation and validation. *Ocean Modelling*, **49-50**: 1-21, <https://doi.org/10.1016/j.ocemod.2012.03.003>.
- Demaria M, Sampson C R, Knaff J A et al. 2014. Is tropical cyclone intensity guidance improving? *Bulletin of the American Meteorological Society*, **95**(3): 387-398, <https://doi.org/10.1175/BAMS-D-12-00240.1>.
- Dudhia J. 1989. Numerical study of convection observed during the winter monsoon experiment using a mesoscale two-dimensional model. *Journal of the Atmospheric Sciences*, **46**(20): 3077-3107, [https://doi.org/10.1175/1520-0469\(1989\)046<3077:NSOCOD>2.0.CO;2](https://doi.org/10.1175/1520-0469(1989)046<3077:NSOCOD>2.0.CO;2).
- Emanuel K. 2017. Will global warming make hurricane forecasting more difficult? *Bulletin of the American Meteorological Society*, **98**(3): 495-501, <https://doi.org/10.1175/BAMS-D-16-0134.1>.
- Emanuel K A. 1999. Thermodynamic control of hurricane intensity. *Nature*, **401**(6754): 665-669, <https://doi.org/10.1038/44326>.
- Ge Z P, Dai Z J, Pang W H et al. 2017. LIDAR-based detection of the post-typphoon recovery of a meso-macrotidal beach in the Beibu Gulf, China. *Marine Geology*, **391**: 127-143, <https://doi.org/10.1016/j.margeo.2017.08.008>.
- Gronholz A, Gräwe U, Paul A et al. 2017. Investigating the effects of a summer storm on the North Sea stratification using a regional coupled ocean-atmosphere model. *Ocean Dynamics*, **67**(2): 211-235, <https://doi.org/10.1007/s10236-016-1023-2>.
- Guan S D, Zhao W, Huthnance J et al. 2014. Observed upper ocean response to typhoon Megi (2010) in the Northern South China Sea. *Journal of Geophysical Research*, **119**(5): 3134-3157, <https://doi.org/10.1002/2013JC009661>.
- Hong S Y, Noh Y, Dudhia J. 2006. A new vertical diffusion package with an explicit treatment of entrainment processes. *Monthly Weather Review*, **134**(9): 2318-2341, <https://doi.org/10.1175/MWR3199.1>.
- Hormann V, Centurioni L R, Rainville L et al. 2014. Response of upper ocean currents to Typhoon Fanapi. *Geophysical Research Letters*, **41**(11): 3995-4003, <https://doi.org/10.1002/2014GL060317>.
- Jacob R, Larson J, Ong E. 2005. M×N Communication and parallel interpolation in community climate system model version 3 using the model coupling toolkit. *The International Journal of High Performance Computing Applications*, **19**(3): 293-307, <https://doi.org/10.1177/109434>

- 2005056116.
- Kain J S. 2004. The Kain-Fritsch convective parameterization: an update. *Journal of Applied Meteorology and Climatology*, **43**(1): 170-181, [https://doi.org/10.1175/1520-0450\(2004\)043<0170:TKCPAU>2.0.CO;2](https://doi.org/10.1175/1520-0450(2004)043<0170:TKCPAU>2.0.CO;2).
- Ko D S, Chao S Y, Wu C C et al. 2014. Impacts of typhoon Megi (2010) on the South China Sea. *Journal of Geophysical Research*, **119**(7): 4474-4489, <https://doi.org/10.1002/2013JC009785>.
- Laprise R. 1992. The Euler equations of motion with hydrostatic pressure as an independent variable. *Monthly Weather Review*, **120**(1): 197-207, [https://doi.org/10.1175/1520-0493\(1992\)120<0197:TEEMOW>2.0.CO;2](https://doi.org/10.1175/1520-0493(1992)120<0197:TEEMOW>2.0.CO;2).
- Large W G, McWilliams J C, Doney S C. 1994. Oceanic vertical mixing: a review and a model with a nonlocal boundary layer parameterization. *Reviews of Geophysics*, **32**(4): 363-403, <https://doi.org/10.1029/94RG01872>.
- Larson J, Jacob R, Ong E. 2005. The model coupling toolkit: a new Fortran90 toolkit for building multiphysics parallel coupled models. *The International Journal of High Performance Computing Applications*, **19**(3): 277-292, <https://doi.org/10.1177/1094342005056115>.
- Liu J L, Cai S Q, Wang S G. 2011. Observations of strong near-bottom current after the passage of Typhoon Pabuk in the South China Sea. *Journal of Marine Systems*, **87**(1): 102-108, <https://doi.org/10.1016/j.jmarsys.2011.02.023>.
- McWilliams J C, Restrepo J M, Lane E M et al. 2004. An asymptotic theory for the interaction of waves and currents in coastal waters. *Journal of Fluid Mechanics*, **511**: 135-178, <https://doi.org/10.1017/S0022112004009358>.
- Mei W, Lien C C, Lin I I et al. 2015. Tropical cyclone-induced ocean response: a comparative study of the South China Sea and tropical Northwest Pacific. *Journal of Climate*, **28**(15): 5952-5968, <https://doi.org/10.1175/JCLI-D-14-00651.1>.
- Mlawer E J, Taubman S J, Brown P D et al. 1997. Radiative transfer for inhomogeneous atmospheres: RRTM, a validated correlated-k model for the longwave. *Journal of Geophysical Research*, **102**(D14): 16663-16682, <https://doi.org/10.1029/97JD00237>.
- Paulson C A. 1970. The mathematical representation of wind speed and temperature profiles in the unstable atmospheric surface layer. *Journal of Applied Meteorology and Climatology*, **9**(6): 857-861, [https://doi.org/10.1175/1520-0450\(1970\)009<0857:TMROWS>2.0.CO;2](https://doi.org/10.1175/1520-0450(1970)009<0857:TMROWS>2.0.CO;2).
- Peduzzi P, Chatenoux B, Dao H et al. 2012. Global trends in tropical cyclone risk. *Nature Climate Change*, **2**(4): 289-294, <https://doi.org/10.1038/nclimate1410>.
- Penven P, Debreu L, Marchesiello P et al. 2006. Evaluation and application of the ROMS 1-way embedding procedure to the central California upwelling system. *Ocean Modelling*, **12**(1-2): 157-187, <https://doi.org/10.1016/j.ocemod.2005.05.002>.
- Pianezze J, Barthe C, Bielli S et al. 2018. A new coupled ocean-waves-atmosphere model designed for tropical storm studies: example of tropical cyclone Bejisa (2013-2014) in the South-West Indian Ocean. *Journal of Advances in Modeling Earth Systems*, **10**(3): 801-825, <https://doi.org/10.1002/2017MS001177>.
- Price J F. 1981. Upper ocean response to a hurricane. *Journal of Physical Oceanography*, **11**(2): 153-175, [https://doi.org/10.1175/1520-0485\(1981\)011<0153:UORTAH>2.0.CO;2](https://doi.org/10.1175/1520-0485(1981)011<0153:UORTAH>2.0.CO;2).
- Price J F. 1983. Internal wave wake of a moving storm. Part I. Scales, energy budget and observations. *Journal of Physical Oceanography*, **13**(6): 949-965, [https://doi.org/10.1175/1520-0485\(1983\)013<0949:IWWOAM>2.0.CO;2](https://doi.org/10.1175/1520-0485(1983)013<0949:IWWOAM>2.0.CO;2).
- Rogers R, Aberson S, Black M et al. 2006. The intensity forecasting experiment: a NOAA multiyear field program for improving tropical cyclone intensity forecasts. *Bulletin of the American Meteorological Society*, **87**(11): 1523-1538, <https://doi.org/10.1175/BAMS-87-11-1523>.
- Salgado R, Soares P, Policarpo C et al. 2015. Summer Boundary Layer structure and circulations in the presence of a large man made lake. In: EGU General Assembly 2015. Vienna, EGU.
- Shchepetkin A F, McWilliams J C. 1998. Quasi-monotone advection schemes based on explicit locally adaptive dissipation. *Monthly Weather Review*, **126**(6): 1541-1580, [https://doi.org/10.1175/1520-0493\(1998\)126<1541:QMASBO>2.0.CO;2](https://doi.org/10.1175/1520-0493(1998)126<1541:QMASBO>2.0.CO;2).
- Shchepetkin A F, McWilliams J C. 2005. The regional oceanic modeling system (ROMS): a split-explicit, free-surface, topography-following-coordinate oceanic model. *Ocean Modelling*, **9**(4): 347-404, <https://doi.org/10.1016/j.ocemod.2004.08.002>.
- Sian K T C L K, Dong C M, Liu H L et al. 2020. Effects of model coupling on typhoon Kalmaegi (2014) simulation in the South China Sea. *Atmosphere*, **11**(4): 432, <https://doi.org/10.3390/atmos11040432>.
- Sun L, Zheng Q A, Tang T Y et al. 2012. Upper ocean near-inertial response to 1998 Typhoon Faith in the South China Sea. *Acta Oceanologica Sinica*, **31**(2): 25-32, <https://doi.org/10.1007/s13131-012-0189-9>.
- Uchiyama Y, McWilliams J C, Shchepetkin A F et al. 2010. Wave-current interaction in an oceanic circulation model with a vortex-force formalism: application to the surf zone. *Ocean Modelling*, **34**(1-2): 16-35, <https://doi.org/10.1016/j.ocemod.2010.04.002>.
- Voldoire A, Decharme B, Pianezze J et al. 2017. SURFEX v8.0 interface with OASIS3-MCT to couple atmosphere with hydrology, ocean, waves and sea-ice models, from coastal to global scales. *Geoscientific Model Development*, **10**(11): 4207-4227, <https://doi.org/10.5194/gmd-10-4207-2017>.
- Weatherford C L, Gray W M. 1988. Typhoon structure as revealed by aircraft reconnaissance. Part I: data analysis and climatology. *Monthly Weather Review*, **116**(5): 1032-1043, [https://doi.org/10.1175/1520-0493\(1988\)116<1032:TSARBA>2.0.CO;2](https://doi.org/10.1175/1520-0493(1988)116<1032:TSARBA>2.0.CO;2).
- Wu R H, Zhang H, Chen D K et al. 2018. Impact of Typhoon Kalmaegi (2014) on the South China Sea: simulations using a fully coupled atmosphere-ocean-wave model.

- Ocean Modelling*, **131**: 132-151, <https://doi.org/10.1016/j.ocemod.2018.08.004>.
- Wu R H, Zhang H, Chen D K. 2020. Effect of Typhoon Kalmaegi (2014) on northern South China Sea explored using Multi-platform satellite and Buoy observations data. *Progress in Oceanography*, **180**: 102218, <https://doi.org/10.1016/j.pocean.2019.102218>.
- Xu D, Li Z Y, Wan Z H et al. 2020. The oceanic responses to Typhoon Rananim on the East China Sea. *Acta Oceanologica Sinica*, **39**(7): 69-78, <https://doi.org/10.1007/s13131-020-1573-5>.
- Yang B, Hou Y J. 2014. Near-inertial waves in the wake of 2011 Typhoon Nesat in the northern South China Sea. *Acta Oceanologica Sinica*, **33**(11): 102-111, <https://doi.org/10.1007/s13131-014-0559-6>.
- Zheng J, Tian J W, Liang H. 2017. Observation of near-inertial internal waves on the continental slope in the northwestern South China Sea. *Journal of Ocean University of China*, **16**(2): 184-190, <https://doi.org/10.1007/s11802-017-3153-7>.
- Zhu T, Zhang D L. 2006. The Impact of the storm-induced SST cooling on hurricane intensity. *Advances in Atmospheric Sciences*, **23**(1): 14-22, <https://doi.org/10.1007/s00376-006-0002-9>.